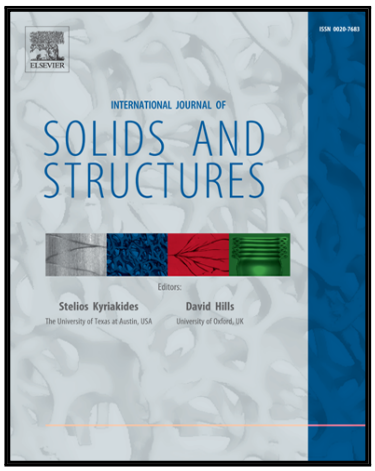

Experimental Verification on Wrinkling Behavior Given by Wrinkling Analysis Using the Tension Field Theory

Takashi Iwasa

PII: S0020-7683(17)30531-0
DOI: 10.1016/j.ijsolstr.2017.11.028
Reference: SAS 9817

To appear in: *International Journal of Solids and Structures*

Received date: 12 January 2017
Revised date: 18 October 2017
Accepted date: 29 November 2017

Please cite this article as: Takashi Iwasa , Experimental Verification on Wrinkling Behavior Given by Wrinkling Analysis Using the Tension Field Theory, *International Journal of Solids and Structures* (2017), doi: 10.1016/j.ijsolstr.2017.11.028

Experimental Verification on Wrinkling Behavior Given by Wrinkling Analysis Using the Tension Field Theory

Takashi IWASA[a]

[a]Department of Mechanical and Aerospace Engineering, Tottori University

4-101, Koyama-cho Minami, Tottori, Japan, 680-8551

Email: iwasa@mech.tottori-u.ac.jp

Corresponding Author: Takashi IWASA

ABSTRACT

This study investigates the physical meaning of membrane surface features given by a wrinkling analysis based on tension field theory and wrinkle strain, which releases the compressive stress in membranes in tension field theory. A rectangular membrane was subjected to shear loading, and the wrinkle geometry and strain field were measured by photogrammetry using a direct linear transformation method. The experimental model was then subjected to a wrinkling analysis based on tension field theory, and the calculated wrinkled membrane behavior was quantitatively compared to the measured results. The analyzed membrane surface features approximately represented the neutral curved surface bisecting the actual wrinkle geometry (the difference was approximately 10% of the maximum wrinkle amplitude), even when the membrane surface feature was not initially flat. The wrinkle strain, defining an in-plane shrinkage strain that releases compressive stress on the membrane in tension field theory, agreed with the experimentally observed in-plane shrinkage strain regardless of the formation process of the wrinkles. The relation between the in-plane shrinkage strain and ratio of the wrinkle amplitude to the half-wavelength of the wrinkles was then derived from inextensional theory. This relation appropriately described the relation measured in the experiment, confirming that inextensional theory describes the wrinkle formation. The results of this study will assist the evaluation of the simulation results using tension field theory for the development of future lightweight, membrane-based space structures such as sunshields and solar sails.

Keywords: Experimental Verification, Membrane Surface Feature, Wrinkle Strain, Tension Field Theory, Photogrammetry

1. INTRODUCTION

Membranes can potentially be assembled into advanced ultra-lightweight space structures with large-area surfaces. For this reason, they have gained increasing attention in recent years. Examples of large membrane space structures are sunshields(Gardner et al., 2006), solar sails(Fu et al., 2016), and a large deployable antenna reflector(Santiago-Prowald and Baier, 2013). However, as membranes are flexible materials, they are easily deformed under small external disturbances. When a membrane is distorted in orbit, the operation function of the membrane space structure is affected. Thus, before launching a reliable large-sized membrane space structure in future, we must predict the nonlinear membrane behavior. However, the membrane behavior is difficult to predict in a ground test because the membrane has a negligible bending stiffness and easily sags under its own weight. For this reason, the membrane space structure must be predicted by a computational approach.

Currently, flexible membrane behaviors (including wrinkles and slacks) are estimated by two representative computational approaches; one based on shell theory (Iwasa et al., 2004; Lee and Lee, 2006; Miyamura, 2000; Senda et al., 2015; Wong and Pellegrino, 2006b; Woo and Jenkins, 2013) and the other by making use of tension field theory (Akita and Natori, 2008; Lu et al., 1998; Miller et al., 1985; Nakashino and Natori, 2006; Roddeman, 1991; Steigmann, 1990; Stein and Hedgepeth, 1961; Wagner, 1931a, b, c; Wong and Pellegrino, 2006b). In the shell theory analysis, a membrane is modeled as a thin shell material; and its nonlinear behavior, such as wrinkling, is treated as a local buckling of the membrane. Accordingly, shell theory analysis can provide the detailed surface features of the membrane, including wrinkles and slacks. The validity of this treatment has been investigated in direct comparisons with experimentally measured surface shapes of the membranes (Lan et al., 2014; Lecieux and Bouzidi, 2010; Miyamura, 2000; Wang et al., 2007; Wong and Pellegrino, 2006a).

In tension field theory, a membrane is modeled as an ideal material with negligible bending stiffness that carries no compressive stresses. The wrinkling behavior is treated as a zero-energy deformation, and is represented by an in-plane shrinkage deformation of membranes. A wrinkle strain, which represents the in-plane shrinkage strain of the wrinkled membrane, immediately releases compressive stress on the membrane. Accordingly, the calculated membrane surface does not reflect the actual membrane behavior, and cannot be directly compared to the experimentally measured surface feature of the membrane. For this reason, tension field theory has been validated by qualitatively comparing the analysis

results with the visually inspected features of the membrane surface, especially the direction of wrinkling and the sizes of the taut, wrinkled and slack regions or by comparing the load–displacement curve given by the experiment and analysis (Mansfield, 1970; Mikulas, 1964; Stein and Hedgepeth, 1961). However, as tension field theory incurs much lower computational cost than shell theory, it is expected to become a practical computational tool predicting the behaviors of large-sized membrane space structures. Under this circumstance, the results can no longer be validated by traditional qualitative discussion, and physical corresponding relations between the simulation results and the actual wrinkled membrane behavior must be quantitatively interpreted.

This paper analyzes the physical meaning of wrinkled membrane behavior given by tension field theory, focusing on the membrane surface features and wrinkle strain. Initially, the wrinkling phenomena on a rectangular membrane under shear loading are investigated by photogrammetry using the direct linear transformation method (Abdel-Aziz, 1971). This technique provides the three-dimensional (3D) position coordinates of the target points embedded on the object surface, enabling quantitative measurements of both the strain field and displacement field. Then, the tension field theory of the experiment model is implemented in a finite element analysis. The nodal positions in the finite element model coincide with the target positions measured by photogrammetry. The experimental membrane surface features provide the initial geometric imperfection of the model, and the measured data become the enforced displacement in the analysis. In this setup, the measured membrane behavior is simulated as faithfully as possible. Finally, the physical corresponding relation between the simulation results and the actual wrinkled membrane behavior is discussed by comparing the simulated and measured results.

The remainder of this paper is structured as follows. Section 2 outlines the experiment and presents the membrane model and configuration of the photogrammetric measurement system. It then explains the calculation of the strain field from the measured displacement data. In section 3, we formulate the finite element analysis and the special membrane element model in terms of tension field theory. Section 4 compares the simulation and experimental results, and discusses the physical meaning of the calculated membrane surface features and wrinkle strain. The paper concludes with a summary of the major findings in Section 5.

2. EXPERIMENT

2.1 Membrane model

The applied membrane model and material parameters of the membrane (DuPont, 2014) are presented in Fig. 1 and Table 1, respectively. The membrane was a (0.15 × 0.15) m^2 piece of polyimide film (Kapton H-type) with a thickness of 25×10^{-6} m. The upper and bottom edges of the membrane were attached to acrylic plates with spray glue. The attachment was performed by a special device that ensured parallel separation of the acrylic plates by 0.15 m. The membrane was printed with a rectangular pattern of 1.0×10^{-3} m-diameter spots, providing target points for the photogrammetry. Measurements were performed over a (0.138 × 0.138) m^2 area of the membrane. The number of target points was 576 (24 × 24 points in the horizontal and vertical directions, respectively).

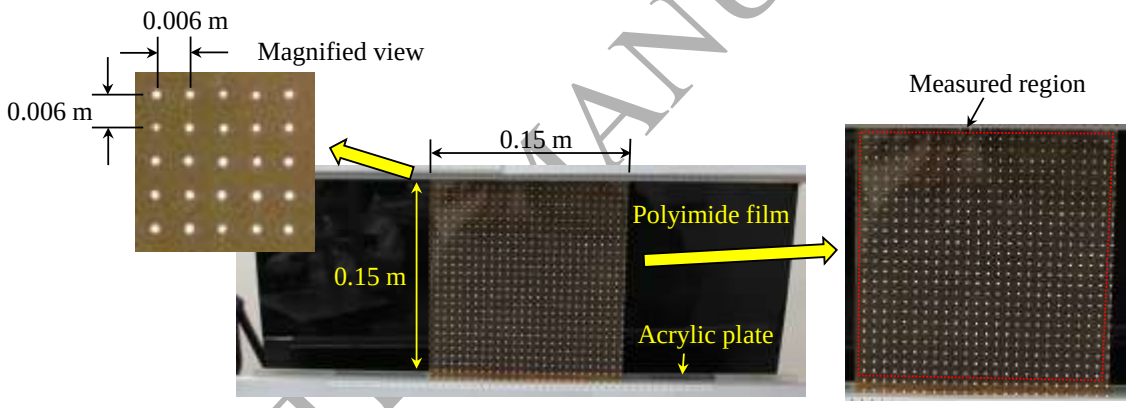

Fig. 1. Membrane model used in this study. The membrane is a polyimide film with an area of (0.15 × 0.15) m^2 and a thickness of 25×10^{-6} m. The membrane surface is imprinted with 576 white circular points, providing target points for the photogrammetry measurements.

Table 1 Material parameters of the membrane (Kapton H-type, DuPont, 2014)

Tensile elastic modulus [MPa]	3400
Poisson's ratio	0.3
Thickness [m]	25×10^{-6}
Tensile strength [MPa]	340

Figure 2 shows the experimental device. The upper clamp bar in Panel (a) is moved vertically or horizontally by two micrometers installed at the backside of the device. To apply a shear loading on the membrane, we moved the upper clamp bar only in the horizontal direction. The bottom clamp bar was fixed on the device. Panel (b) shows the installation of the membrane between the acrylic plates affixed to the two clamp bars. The membrane surface was wrinkled by moving the upper clamp bar in the horizontal direction. To clearly capture the white target points by digital cameras, we placed a black board behind the membrane.

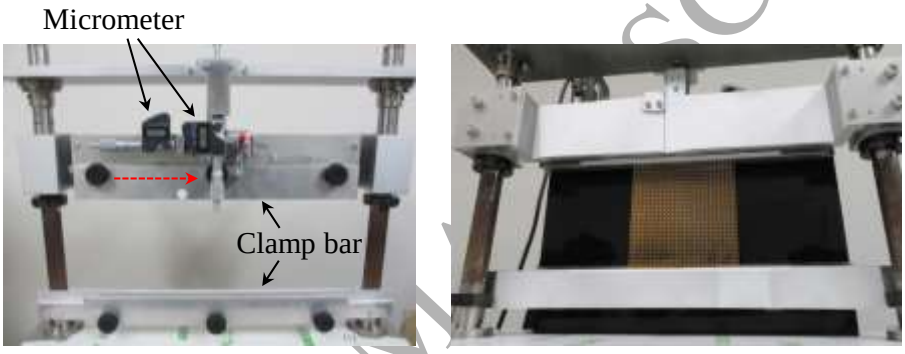

(a) Back side (b) Adverse side

Fig. 2. Experimental device: (a) backside view, and (b) adverse side view. The upper clamp is moved by two micrometers installed on the backside of the device. The acrylic plates holding the membrane are affixed by the upper and lower clamp bars.

2.2 Measurement configuration

Panels (a) and (b) of Fig. 3 show the configuration of the photogrammetric measurement and the alignment of the digital cameras and object, respectively. The parameters θ_{ij} and d_i in the Fig. 3 (b) are listed in Table 2, and the digital camera specifications are listed in Table 3. The experimental device was installed approximately 0.4 m in front of the four digital cameras. In this digital camera alignment, the optical axis of each camera was angled in the 20°–25° range, and the physical size of the pixels in the image data was approximately 0.1×10^{-3} m. The photogrammetry was calibrated using a single−axis spindle stage placed at one side of the experimental device.

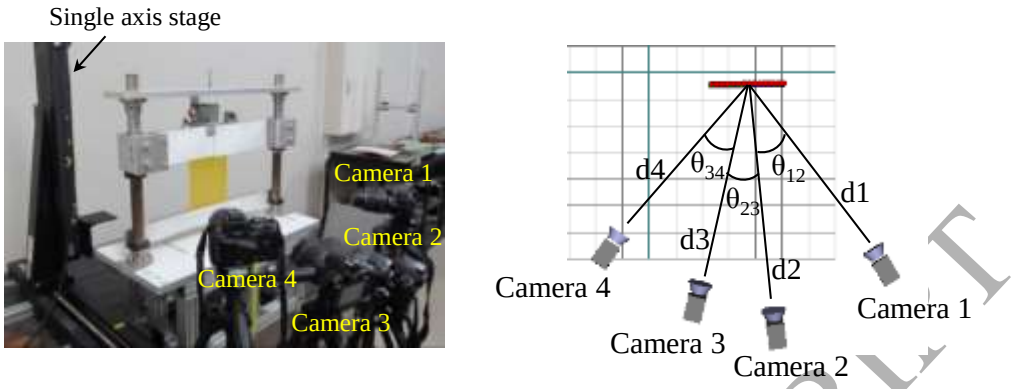

(a) Measurement situation (b) Arraignment of the four digital cameras

Fig. 3. Measurement configuration. Four digital cameras are installed in front of the membranes. Panels (a) and (b) present the situation of the photogrammetric measurement system and the alignment of the measurement equipment, respectively.

Table 2 Alignment parameters of the four digital cameras

Distance between digital camera and object				Angle between adjacent cameras		
d1	d2	d3	d4	θ_{12}	θ_{23}	θ_{34}
0.437 m	0.471 m	0.428 m	0.412 m	22 deg.	23 deg.	25 deg.

Table 3 Specifications of the digital cameras

Model	Nikon D3000 (Single-lens reflex camera)
Image pickup device	21.3 × 15.8 mm^2 size CCD sensor
Effective sensor resolution	3872 × 2592 $pixel^2$
Shutter speed	1/6 s
Aperture value	F22
Zoom ring	18

2.3 Calibration of photogrammetric measurement system

Photogrammetry by the direct linear transformation method is a non-contact, full-field surface−shape measurement method. Using a triangulation technique, it

extracts the 3D position coordinates of the target points embedded on the object surface from multiple images acquired at different perspectives. The linear transformation method requires several parameters, called intrinsic and extrinsic camera parameters, which must be initially determined. These parameters are generally calculated by measuring the control points with known 3D position coordinates; that is, by calibrating the photogrammetric measurement system.

Figure 4 shows the alignment of the control points in the calibration procedure. The eight control points represent the corners of a rectangular parallelepiped sized (0.4 × 0.2 × 0.05) m^3. The interior of the rectangular parallelepiped defines the measurement space of the photogrammetry. The photogrammetry was performed in a Cartesian coordinate system with origin located at the back left corner of the parallelepiped. In this study, the control points were created using a dedicated calibration jig composed of a flat plate and two perpendicularly arranged single−axis spindle stages (see Fig. 5). The flat plate was installed on the vertical spindle stage. The side of the flat plate was engraved with two 1.2×10^{-3} m-diameter control points separated by 0.4 m. During the calibration, the two spindle stages were moved in the order of the numbers written in Fig. 5. The intrinsic and extrinsic camera parameters were then determined from photographs of the two control points taken by the four digital cameras, yielding eight control points. The standard deviation of the eight control points in the calibration was 0.02×10^{-3} m. The specifications of the single−axis spindle stage are listed in Table 4.

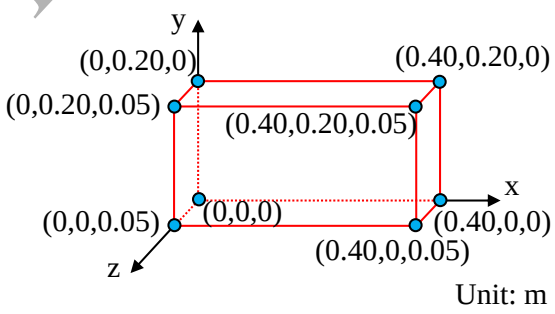

Fig. 4. Alignment of the eight control points in the photogrammetry calibration.

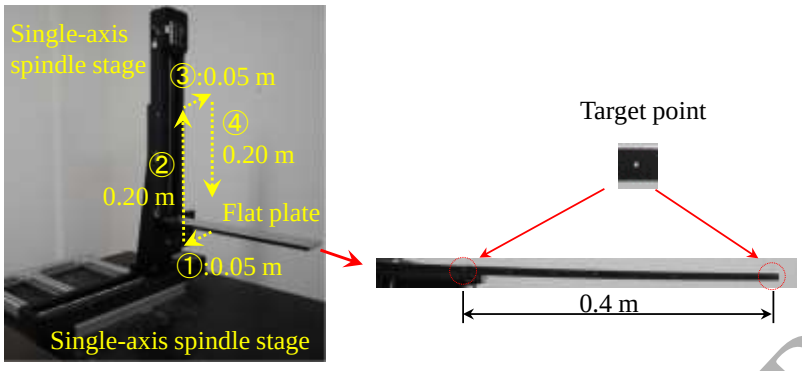

Fig. 5. Calibration jig composed of two perpendicular single−axis spindle stages and a flat plate. The flat plate on the vertical spindle stage has two control points separated by 0.4 m. By moving the single−axis spindle stages in the order of the yellow numbers, we precisely determine the eight control points.

Table 4 Specifications of the single−axis spindle stages

Model	SIGMA KOKI SGSP46-500
Maximum displacement	±0.25 m
Positional repeatability	6×10^{-6} m
Straightness	20×10^{-6} m

2.4 Surface shape measurement of the wrinkled membrane

After completing the calibration, we measured the surface shape in the experimental model. Initially, the experimental device was installed (as far as possible) with its upper and lower clamp bars parallel to the x–y plane in the Cartesian coordinate system of the photogrammetry. The upper clamp bar was then displaced by 0.8×10^{-3} m in the x direction with a micrometer, at incremental displacements of 0.05×10^{-3} m. During the loading, the wrinkling phenomena on the membrane surface were captured by the four digital cameras. After the measurement, the 3D position coordinates of the target points on the membrane surface were calculated from the captured image data using the commercial software Move TR 3D (Library Co., Ltd.).

The preliminary measurement confirmed that a measurement accuracy of approximately 15×10^{-6} m in the x and y directions of the photogrammetric measurement system, and 30×10^{-6} m in the z direction in our laboratory

environment. This measurement accuracy was obtained by measuring the movement of the target points embedded in the rigid plate board attached to the experimental device in Fig. 2. The movement of the rigid plate board was precisely controlled by the micrometers; therefore, the measurement accuracy was determined by comparing the results of photogrammetry and the movement of the rigid plate board.

2.5 Calculation of strain field

To physically interpret the membrane surface features and wrinkle strain given by the tension field theory analysis, we must compare both the strain and displacement fields with the experimentally measured values. As the direct linear transformation method in photogrammetry provides only the 3D position coordinates of the target points embedded on the membrane surface, we must calculate the strain field on the membrane surface separately from the measured data, subject to the following three requirements.

(1) The type of measured strain must match that used in the tension field theory analysis.
(2) The output locations of the measured strain must coincide with the analytical strain positions.
(3) The strain is calculated by the same algorithm as the analysis.

In the finite element analysis formulation of tension field theory (see Section 3), the Green–Lagrange strain is calculated in generalized curvilinear coordinates, then transformed to Cartesian coordinates centralized in a four-node quadrilateral element. The experimental strains are calculated by the same algorithm.

The generalized curvilinear coordinate system embedded in the membrane surface is illustrated in Fig. 6. In this coordinate system, the covariant component of the Green–Lagrange strain is the difference between the metric tensors defined in the deformed and initial configurations of the membrane (denoted by g_{ij} and G_{ij}, respectively). The Green–Lagrange strain is then given by

$$\boldsymbol{E} = \frac{1}{2}\left(g_{ij} - G_{ij}\right)\boldsymbol{G}^i \otimes \boldsymbol{G}^j \quad (i,j = 1,2), \tag{1}$$

where the two metric tensors are given as follows.

$$G_{ij} = \mathbf{G}_i \cdot \mathbf{G}_j \tag{2}$$

$$g_{ij} = \mathbf{g}_i \cdot \mathbf{g}_j \tag{3}$$

By definition,

$$\mathbf{G}_i = \frac{\partial \boldsymbol{X}}{\partial r^i} \tag{4}$$

$$\mathbf{g}_i = \frac{\partial \boldsymbol{x}}{\partial r^i} = \frac{\partial \boldsymbol{X}+\boldsymbol{u}}{\partial r^i} = \mathbf{G}_i + \frac{\partial \boldsymbol{u}}{\partial r^i} \tag{5}$$

where r^i denotes the axes in the generalized curvilinear coordinates system. Substituting Eqs. (4) and (5) into Eq. (1), the Green–Lagrange strain becomes

$$\boldsymbol{E} = \frac{1}{2}\left(\frac{\partial \boldsymbol{u}}{\partial r^i} \cdot \boldsymbol{G}_j + \boldsymbol{G}_i \cdot \frac{\partial \boldsymbol{u}}{\partial r^j} + \frac{\partial \boldsymbol{u}}{\partial r^i} \cdot \frac{\partial \boldsymbol{u}}{\partial r^j}\right) \boldsymbol{G}^i \otimes \boldsymbol{G}^j. \tag{6}$$

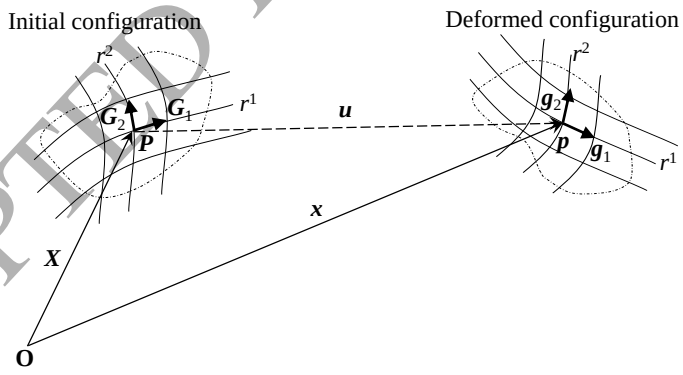

Fig. 6. Concept of generalized curvilinear coordinate system embedded in the membrane surface. X and x are position vectors indicating an arbitrary particle P on the membrane surface. u is the displacement vector from P on the initial configuration to p on the deformed configuration. G_i and g_i are defined in the text. r^1 and r^2 are the axes in the generalized two-dimensional curvilinear coordinate system.

Considering the target points on the membrane surface as the nodal points in

the analysis, we constructed four-node quadrilateral elements for the experiment model, similar to those constructed in the analysis. Figure 7 illustrates a quadrilateral element composed of four target points. The r^1 and r^2 axes define the neutral coordinate system in each element. The 3D position coordinates and the displacement of an arbitrary point in the quadrilateral element can be written in the terms of the shape functions N^n of the element:

$$\boldsymbol{X} = N^n \cdot \boldsymbol{X}^n \tag{7}$$

$$\boldsymbol{u} = N^n \cdot \boldsymbol{u}^n, \tag{8}$$

where n $(n = 1 - 4)$ are the indices of the target points in the quadrilateral element, and $\boldsymbol{X}^n$ and $\boldsymbol{u}^n$ are the measured photogrammetry data. The shape functions N^n of the element are given by the following expressions.

$$N^1 = \frac{1}{4}(1 - r^1)(1 - r^2) \tag{9}$$

$$N^2 = \frac{1}{4}(1 + r^1)(1 - r^2) \tag{10}$$

$$N^3 = \frac{1}{4}(1 + r^1)(1 + r^2) \tag{11}$$

$$N^4 = \frac{1}{4}(1 - r^1)(1 + r^2), \tag{12}$$

where r^1 and r^2 vary from −1 to +1. Substituting Eqs. (7), (8), and (4) into Eq. (6), we obtain the covariant component of the Green–Lagrange strain at an arbitrary point in the quadrilateral element from the measured data. By transforming the generalized curvilinear coordinate system into the Cartesian coordinate system, we finally obtain the Green–Lagrange strain in Cartesian coordinates. The coordinate transformation is derived from the following relation:

$$\boldsymbol{E} = E_{ij}\boldsymbol{G}^i \otimes \boldsymbol{G}^j = \bar{E}_{kl}\boldsymbol{e}_k \otimes \boldsymbol{e}_l \ . \tag{13}$$

From Eq. (13), the Green–Lagrange strain in Cartesian coordinates is given by

$$\bar{E}_{kl} = E_{ij} \cdot \left(\boldsymbol{G}^i \boldsymbol{e}_k\right)\left(\boldsymbol{G}^j \boldsymbol{e}_l\right). \tag{14}$$

Here, the contravariant base vector $\boldsymbol{G}^i$ is written in terms of the covariant base vector as follows:

$$\mathbf{G}^1 = \frac{\mathbf{G}_2 \times \mathbf{G}_3}{(\mathbf{G}_1 \times \mathbf{G}_2) \cdot \mathbf{G}_3}, \quad \mathbf{G}^2 = \frac{\mathbf{G}_3 \times \mathbf{G}_1}{(\mathbf{G}_1 \times \mathbf{G}_2) \cdot \mathbf{G}_3}. \tag{15}$$

where

$$\mathbf{G}_3 = \frac{\mathbf{G}_1 \times \mathbf{G}_2}{|\mathbf{G}_1 \times \mathbf{G}_2|} \ . \tag{16}$$

$\boldsymbol{e}_l$ in Eq. (14) is a base vector defined in Cartesian coordinates. In this study, the Cartesian Green–Lagrange strain was output at the center of the quadrilateral element and compared with the analytical results. As tension field theory cannot determine the out-of-plane displacement in the wrinkled region, the strain field given by the wrinkling analysis was mainly calculated from the in-plane displacement of the wrinkled membrane. Thus, the experimental strain field was calculated from the in-plane displacement of the measured data, and was compared to the analytical wrinkle strain.

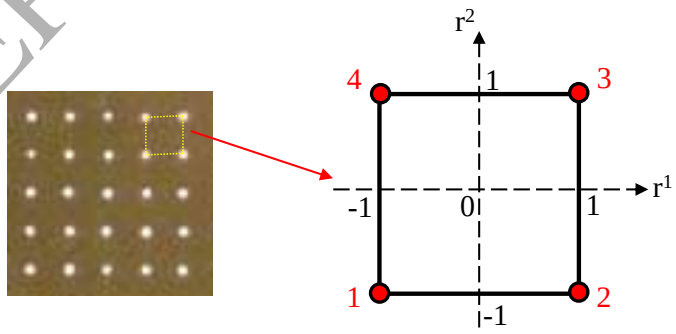

Fig. 7. A quadrilateral element composed of four target points. r^1 and r^2 are axes in the natural coordinate system. The numbers 1–4 of the target points denote the local numbers of each element.

3. ANALYSIS

3.1 Analysis model

Figure 8 shows the membrane model used in the analysis. The mesh division was designed to align the positions of the nodal points with the target points measured by photogrammetry. The measured 3D position coordinates of the target points prior to the shear loading were assigned as the initial geometrical imperfections in the analysis model. The initial stresses induced by the installation of the membrane were not incorporated into the analysis model assuming that weak stresses remained in the membrane and affected the wrinkling behavior appearing on the membrane (Nayyar et al., 2014). Thus, the created analysis model includes uncertainties related to (a) the initial stresses, (b) the measurement of the 3D coordinates of the target points and (c) the lack of the control in the positioning of the membrane on the experimental device. As the measured target points were located inside of the boundary (edge of the acrylic plate) as shown in Fig. 1, the nodal points were newly created at 6.0×10^{-3} m above and below the measured region(in the *y* direction). The *x* and *z* coordinates of the created nodal points were those of the target points at the upper and bottom edges of the measured region. On the lower and upper edges, the new nodal points were perfectly fixed and horizontally displaced by 0.8×10^{-3} m, respectively. The analytical model contained 624 (24 horizontal × 26 vertical) nodal points over an area of (0.138×0.15) m^2 with a thickness of 25×10^{-6} m.

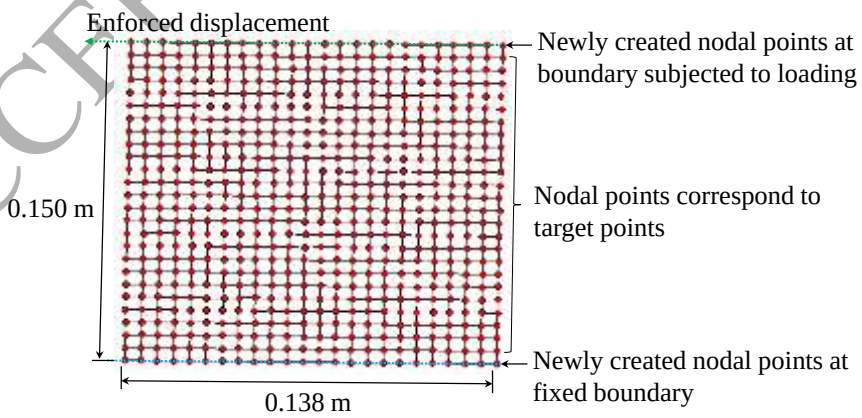

Fig. 8. Analysis model. The 3D positions of the nodal points correspond to the target points measured by photogrammetry. Additional displaced and fixed nodal points

are placed along the top and bottom boundaries, respectively.

3.2 Finite element analysis using tension field theory

The measured wrinkling phenomena were simulated in a finite element analysis of four-node quadrilateral membrane elements based on tension field theory. The analysis was performed by the commercial software FEAP ver.8.4 (Zienkiewicz et al., 2005) developed by Taylor. As membrane elements based on tension field theory are not accommodated by FEAP, they were incorporated into FEAP via a user element function. In this study, the membrane element, which releases a compressive stress on the membrane by a modified elastic-plane stress-constitutive model (Akita , 2004, Akita et al., 2007), was applied. Equation (17) computes the elasticity matrix in the element.

$$\bar{C} = \frac{E}{1-v^2}\begin{bmatrix} a_2-(1-a_1)v^2 & a_1a_2v & 0 \\ a_1a_2v & a_1a_2 & 0 \\ 0 & 0 & G^a \end{bmatrix}, \tag{17}$$

where

$$G^a = \frac{1-v}{2}\left[a_2+(1-a_1)\frac{v\varepsilon_1+\varepsilon_2}{\varepsilon_1-\varepsilon_2}\right] \quad , \tag{18}$$

ε_1 and ε_2 are the major and minor principal strains respectively, and the values of the parameters a_1 and a_2 are conditional on the strain field of the membranes.

1) $\varepsilon_2 + v\varepsilon_1 \geq 0$: Taut regions

$$a_1 = 1, a_2 = 1 \tag{19}$$

2) $\varepsilon_1 \leq 0$: Slack regions

$$a_1 = 1, a_2 = 0 \tag{20}$$

3) $\varepsilon_2 + v\varepsilon_1 < 0, \quad \varepsilon_1 > 0$: Wrinkled regions

$$a_1 = 0, a_2 = 1 \tag{21}$$

The Newton–Raphson method with a line-searching algorithm was used in the finite element analysis. The strain at the center of each element was computed as a

one-point Gaussian integral through the element, while a perfect Gaussian integral was performed during the analysis. The wrinkle strain was then calculated as

$$\varepsilon_w = \varepsilon_2 + \nu\varepsilon_1. \tag{22}$$

In this analysis, some tensile stresses always appear in at least one of the perfect (four-point) Gaussian integral points during the simulation. Therefore, singularity of the tangent stiffness matrix did not occur, and the converged solutions were obtained in all the steps. However, the one-point Gaussian integral was applied to output the results; therefore, some elements carrying no stresses appeared in the analysis results, and some slack regions were observed in the wrinkled membranes as stated subsequently.

4. RESULTS AND DISCUSSION

4.1 Physical meaning of membrane surface feature given by tension field theory

Figure 9 shows the formation process of the wrinkles appearing on the membrane surface subjected to a shear loading. Panel (a) presents photographs of the membrane surface taken by the digital camera, and (b) displays the photogrammetry results. Panel (c) shows the analysis results based on tension field theory. Panels (a) and (b) confirm that the membrane surface was already disturbed in the initial state. In this situation, a displacement of the upper side of the membrane ($d = 0.05$ mm) immediately generated a single wrinkle along the diagonal line (black region in panel (b)) flanked by two slightly slack regions. As the displacement was incrementally increased to $d = 0.4$ mm, two additional wrinkles appeared at one side of the first wrinkle. In the final configuration of the membrane surface, the amplitude of the wrinkles increased. The results confirmed that the membrane surface condition, appearing the main part of the wrinkled regions and slack regions, was roughly decided at the first stage. The new wrinkles formed in the vicinity of the initial wrinkles along the membrane diagonal.

On the other hand, no surface wrinkles appear in the analysis results of Fig. 9 (c) because tension field theory assumes negligible bending stiffness of the membrane. However, the membrane surface deformed from the first stage of the enforced displacement. Qualitatively, this deformation process, which yields the main part of the wrinkled regions in the center of the membrane and slack regions in the edge of the membrane, resembles the experimentally observed membrane behavior.

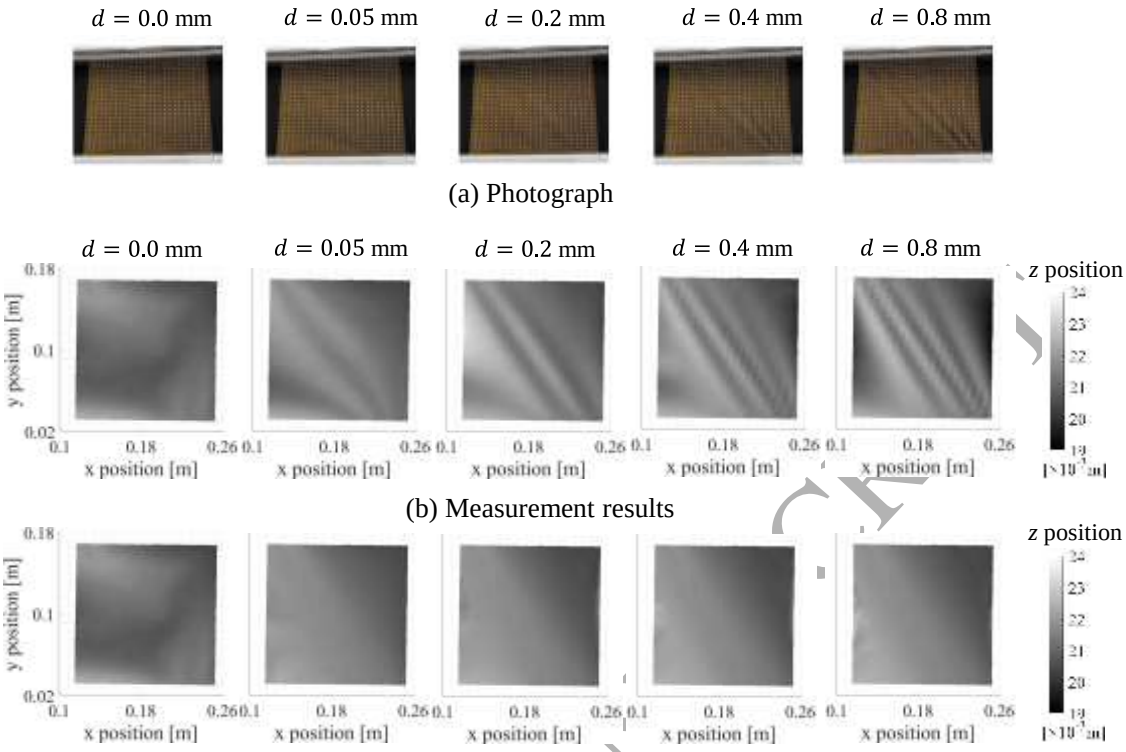

Fig. 9. Formation process of wrinkles appearing on the rectangular membrane subjected to shear loading. The upper side of the membrane is displaced by 0.8×10^{-3} m. Shown are (a) photographs taken by the digital camera, (b) the results of photogrammetry using the direct linear transformation method, and (c) the analysis results based on tension field theory.

Figure 10 profiles the central cross sections of the wrinkled membrane in the *x* direction, obtained in the experiment and analysis. The region labeled *wrinkled region* indicates the wrinkling results of the analysis. In panel (a), a membrane displacement elevates the membrane surface above its initial profile, and a single wrinkle forms near the center of the cross section. The analytical results reveal a similar overall elevation of the membrane surface near the middle surface bisecting the created wrinkle. Additional displacement clarifies this corresponding relation in which the analytical results are located near the middle surface bisecting the wrinkles. Accordingly, we infer that the calculated membrane surface feature in the wrinkled region physically represents the neutral surface bisecting the wrinkle geometry, regardless of the formation process of the wrinkles.

On the contrary, the profiles of the slack regions largely deviate between the analytical and the experiment results as the displacement increases. As the slack

region carries no internal stresses and behaves like a rigid material, its deformation is largely influenced by the deformation of the nearby wrinkles. Tension field theory, which cannot simulate the actual wrinkle deformations, cannot easily replicate this slack behavior. Consequently, the analyzed deformation in the slack region increasingly departs from the experimental deformation as the displacement increases.

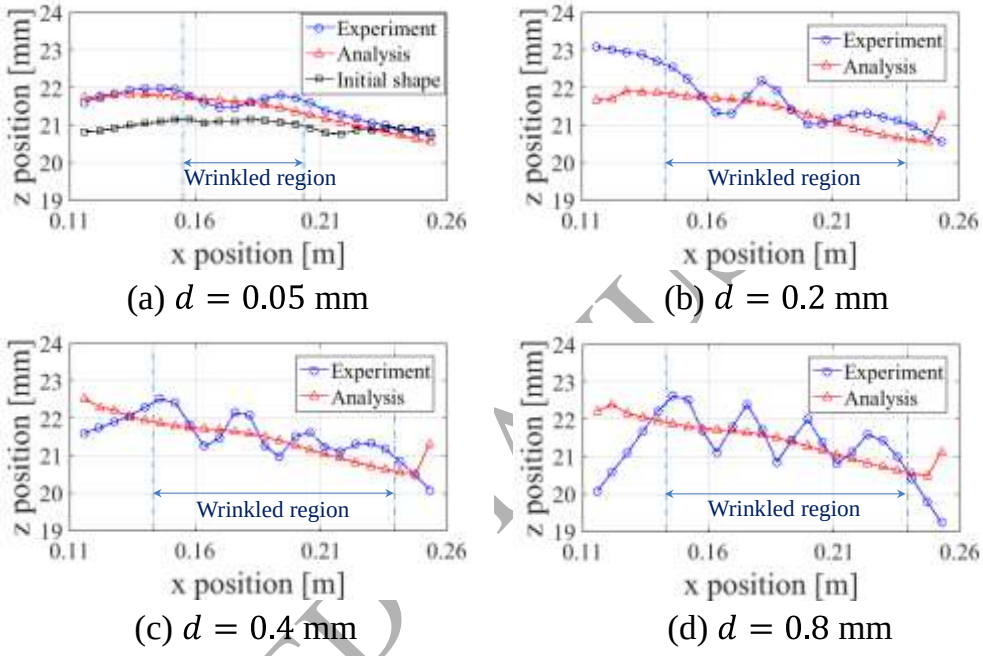

(a) $d = 0.05$ mm (b) $d = 0.2$ mm

(c) $d = 0.4$ mm (d) $d = 0.8$ mm

Fig. 10. Experimental (blue) and analyzed (red) central cross-sectional profiles of a wrinkled membrane displaced by various distances.

Figure 11 compares the central cross-sectional profiles of the neutral surface derived from the least-mean-squares approximation of the wrinkle geometry, and those of the membrane surface calculated by tension field theory. The membrane surface features approximately agree between the two methods. The difference is caused by (a) the different number of sampling data selected for the least-mean-squares approximation, (b) the uncertainties included in the analysis model and (c) the effects of the experimental boundary condition, as stated later.

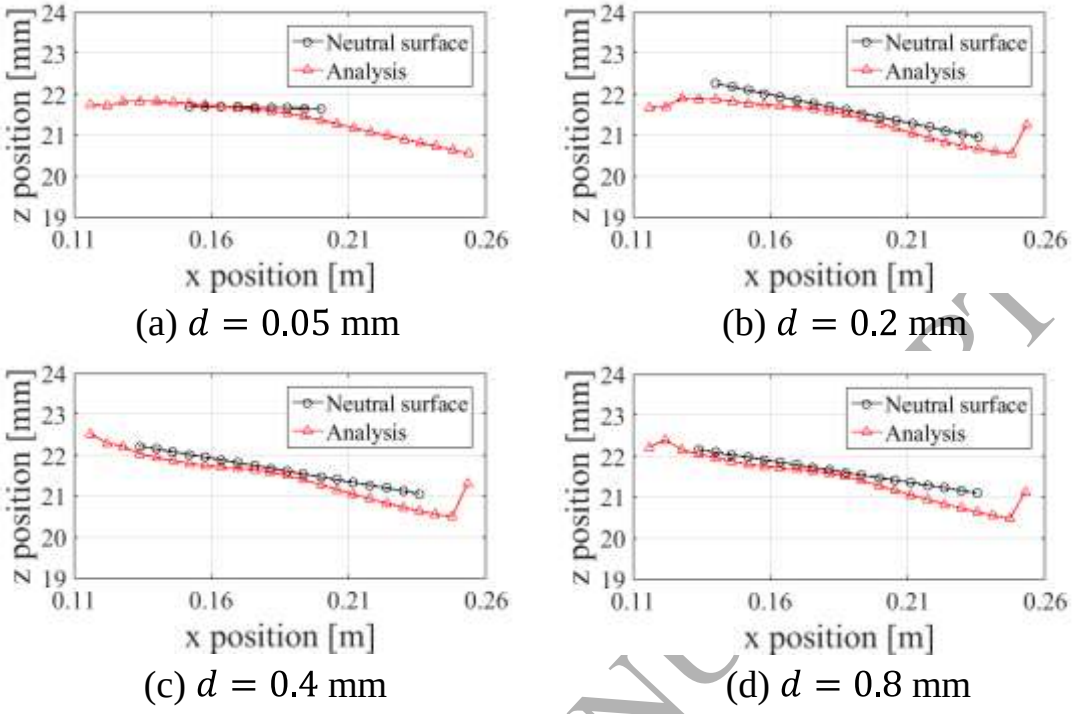

(a) $d = 0.05$ mm (b) $d = 0.2$ mm

(c) $d = 0.4$ mm (d) $d = 0.8$ mm

Fig. 11. Comparison between the central cross-sectional profiles of the membrane surface computed in the analysis (red) and the neutral surface given by the least-mean-squares approximation of the wrinkle geometry. The analytical results approximately agree with the neutral surface.

Figure 12 plots the difference between the membrane surface features computed by tension field theory and the neutral surface given by the least-mean-squares approximation of the wrinkle geometry. The difference is calculated from the surface features of the final membrane ($d = 0.8$ mm) as follows:

$$\delta z_y = \sqrt{\frac{1}{N_y}\left[\sum_{i=1}^{N_y}\left\{z_y^{tft}(i) - z_y^{exp}(i)\right\}^2\right]}\ , \tag{23}$$

where δz_y is the difference on cross section y, N_y is the number of nodal points (target points) in the wrinkled region of each y, and $z_y^{tft}(i)$ and $z_y^{exp}(i)$ denote the analytically calculated z coordinate of the membrane and the measured z coordinate of the neutral surface, respectively, at nodal point i on cross section y.

Each *y* coordinate along the abscissa of Fig. (12) is a location along the cross section of the membrane. The ordinate is the difference given by Eq. (23). Note that the difference increases sharply near the bottom edge of the membrane (i.e., from y = 0.03 m to y = 0.05 m), and is maximized in the middle region. The maximum difference is approximately 10% of the maximum amplitude of the wrinkles (1.7×10^{-3} m).

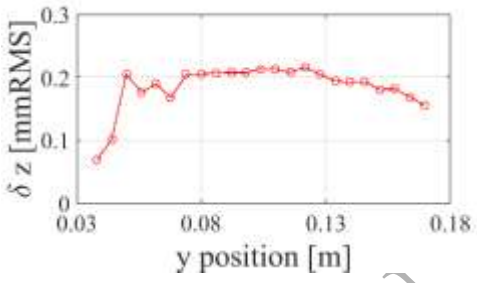

Fig. 12. Difference between the final membrane surface features ($d = 0.8$ mm) given by tension field theory and the neutral surface bisecting the wrinkle geometry. The *y* position denotes a distance along the cross section of the membrane.

Panels (a) and (b) of Fig. 13 show the experimental and numerical displacement distributions, respectively, in the *y* direction at the final state of the membrane ($d = 0.8$ mm). In panel (a), the membrane is displaced from the diagonal line toward the bottom in the right region, and toward the top in the left region. This overall deformation also appears in the analytical results. However, the analysis underestimated the magnitude of the downward displacement (black region in the figure). This discrepancy is attributed to the imperfectly fixed membrane boundary in the experiment, which slightly slips under the enforced displacement. The displacement in the *y* direction certainly differs in the out-of-plane membrane displacements, where the overall deflection of the membrane surface largely deviates from the analytical results. This result partly explains why the membrane surface calculated by tension field theory locates below the neutral surface bisecting the wrinkle geometry (see Figs. 11 and 12).

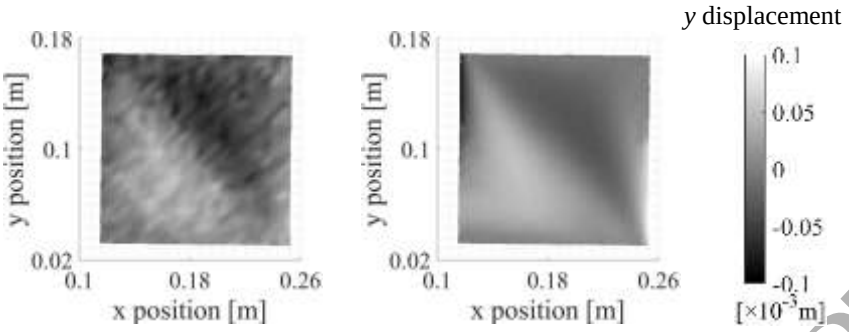

(a) Experiment (b) Analysis

Fig. 13. Displacement distributions in the y direction at the final state of the membrane ($d = 0.80$ mm). Relative to the diagonal line, the right and left regions of the membrane surface are displaced toward the bottom and top sides, respectively, while the magnitude of the displacement is different.

Figure 14 shows the variation of the difference between the calculated and neutral membrane surfaces as the enforced displacement increases. Results are plotted for three cross-sections (y = 0.1038 m, 0.1397 m, and 0.1639 m). The difference increases during the early displacements and remains approximately constant under displacements exceeding $d = 0.2$ mm. Recall that in both experiment and analysis, the first loading determines the membrane surface condition, appearing the main part of the wrinkled regions and slack regions, was roughly decided at the first stage. The difference between the analytical and neutral membrane behaves in a similar way.

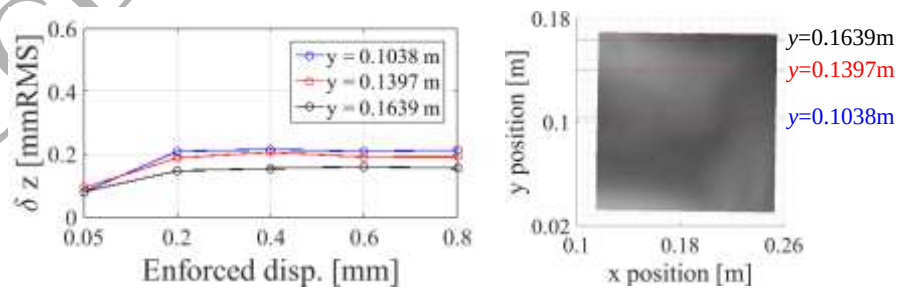

Fig. 14. Variations of the difference between the membrane surface determined by tension field theory and the neutral surface (left panel), determined for three cross-sectional profiles (right panel).

From the above discussion, we infer that the calculated membrane surface features in the wrinkled region were physically located in the vicinity of the neutral surface given by the least-mean-squares approximation of the wrinkle geometry, regardless of the formation of wrinkles. These two membrane surface features differ by roughly 10% of the maximum wrinkle amplitude. These differences were attributed to the imperfectly fixed boundary of the membrane in the experimental setup. On the other hand, the analysis cannot properly model the slack behavior, because this behavior depends on the wrinkle deformations near the slack regions, which cannot be properly treated by tension field theory.

4.2 Physical meaning of the wrinkle strain defined in tension field theory

Figure 15 shows distributions of the major principal strains calculated by tension field theory. The membrane surface deformations were measured in the experiment. From the results, the major principal strain roughly coincides with the wrinkle lines at the first stage ($d = 0.05$ mm), while it is slightly away from the wrinkle lines with increasing the enforced displacement. Especially, the direction angle of the major principal strain tends to large compared to that of the wrinkle lines. The reason why the major principal strain does not completely align with the wrinkle lines is attributed to the imperfectly fixed membrane boundary in the experiment, which slightly slips under the enforced displacement as stated above. In this section, the physical meaning of the wrinkle strain is quantitatively investigated by comparing the analytical and experimental results.

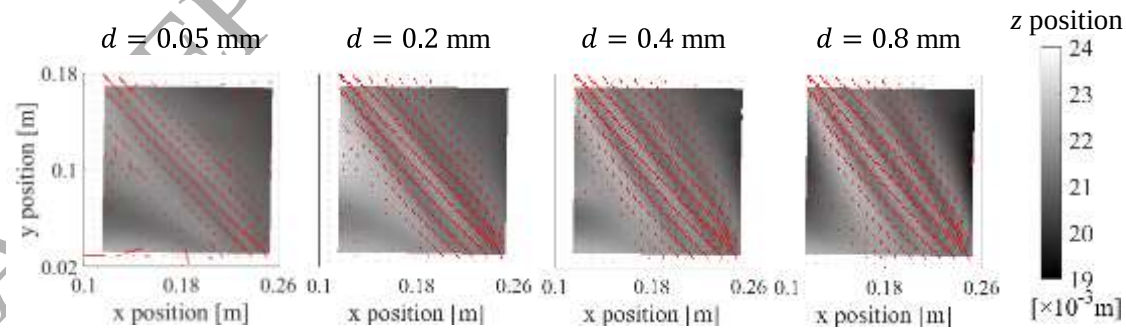

Fig. 15. Distributions of the major principal strains calculated in the analysis. The membrane deformations were experimentally determined. The figure presents the final state of the membrane. The lengths and directions of the red lines indicate the magnitudes and directions of the major principal strains, respectively, calculated by tension field theory. The major principal strains occur on the wrinkles.

Figure 16 shows the spatial distributions of the measured in-plane shrinkage strains and the calculated wrinkle strains. The in-plane shrinkage strain was calculated from the measured displacement data in the *x* and *y* directions. With increasing enforced displacement, the in-plane shrinkage strain intensifies along the membrane diagonal, where the original wrinkles appeared (Fig. 16 (a)). Similar behavior appears in the wrinkle strain distribution given by the analysis. Although the distribution properties slightly disagree, the magnitudes of the analytical and experimental strains are almost identical. The discrepant distribution properties are attributed to measurement errors in the photogrammetry and the slightly unfixed boundary condition of the membrane, as stated before.

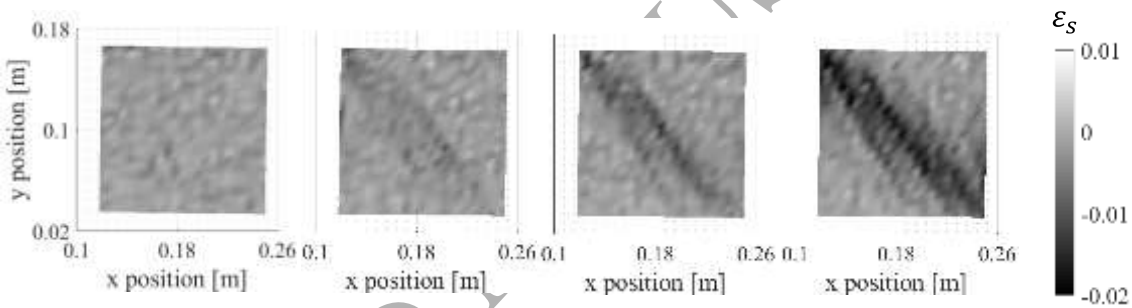

(a) In-plane shrinkage strain measured in experiment

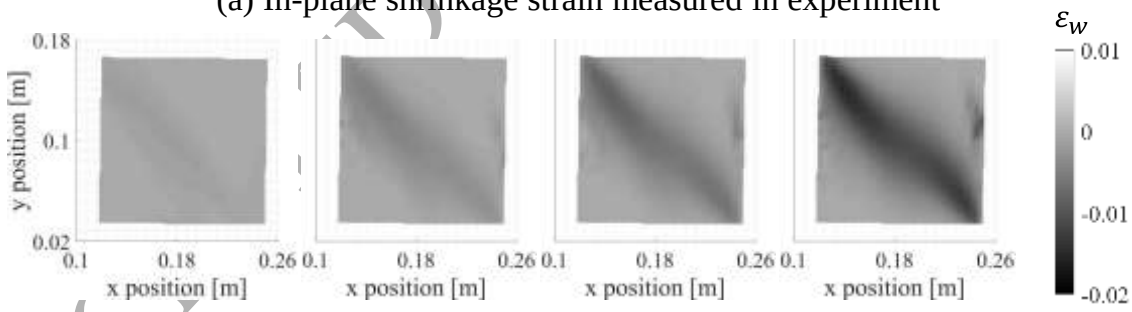

(b) Wrinkle strain given by analysis

Fig. 16. Spatial distributions of the measured in-plane shrinkage strains (top) and the calculated wrinkle strains (bottom).

Figure 17 compares the central cross-sectional distributions of the in-plane shrinkage strain and the wrinkle strain in the wrinkled regions. The central cross-sectional profile of the measured membrane surface is also plotted. Because the strain is the gradient of the displacement field and is highly sensitive to the

measurement error, the shrinkage strain calculated from the measured displacement has a non-smooth distribution. Therefore, to smooth the irregular distribution, the calculated shrinkage strain was subjected to Wiener filtering using MATLAB's wiener2 function (ver. 2016). Assuming a relatively smooth strain field on the wrinkled membrane, the mask size of the Wiener filter was set to 5 points × 5 points (24 mm × 24 mm). The smoothed shrinkage strain in the figure indicates the results. From the figure, the analytically determined distributions of the wrinkle strain approximate those of the measured in-plane shrinkage strains, regardless of the formation process of the wrinkles. The smoothed in-plane shrinkage strain is minimized in the regions of maximum wrinkle amplitude along the central cross section. According to tension field theory, the strong agreement between the in-plane shrinkage strain and wrinkle strain indicates that the membrane can physically carry negligible compressive stress in the wrinkled region. From the results, the formation mechanics of the wrinkles are considered to obey inextensional theory, and the wrinkles should be amplified by contracting the membrane in the in-plane direction. The results in Fig. 17 roughly support the inextensional hypothesis.

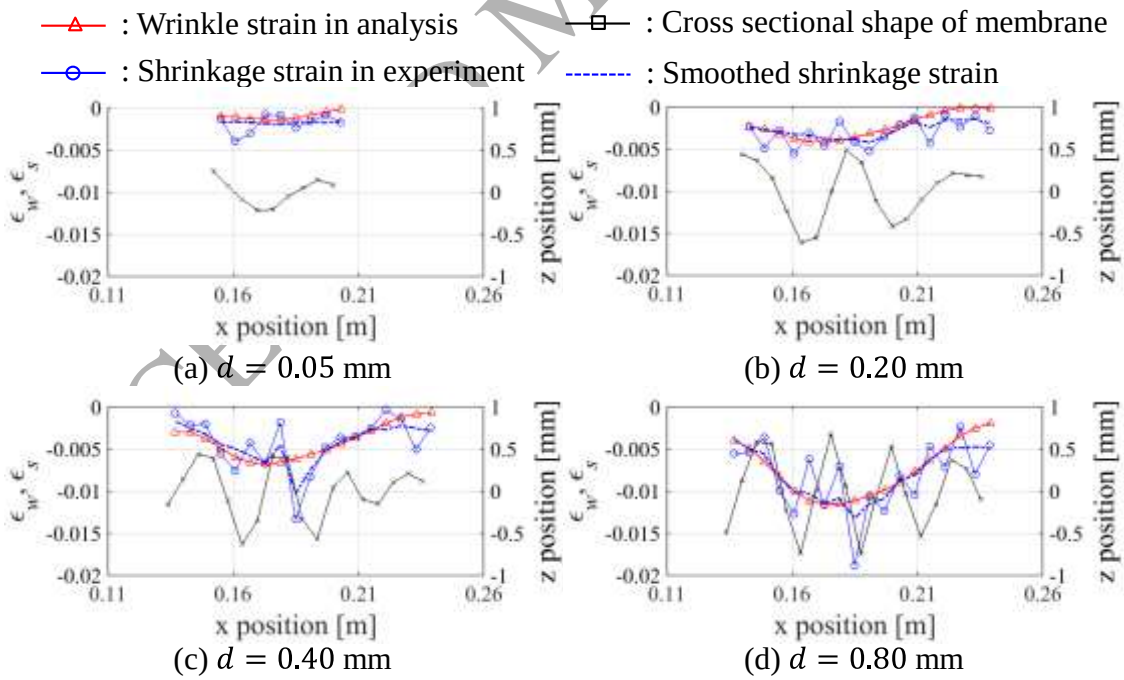

Fig. 17. Comparison of the central cross-sectional distributions of the in-plane shrinkage strain (blue) and the wrinkle strain (red) in the wrinkled region of the membrane, and the measured central cross-sectional profile of the membrane (black).

Abscissa and right ordinate indicate the x and z positions of the membrane, respectively.

Thus, assuming that the wrinkle formation is described by inextensional theory, a relation of the in-plane shrinkage strain to the wrinkle geometry was formulated. Representing a single wrinkle geometry by a half sine wave (Fig. 18), the length along the wrinkle geometry is given

$$l = \int_0^{\lambda} \sqrt{1 + \left(\frac{\partial w}{\partial x}\right)^2}\, dx \ , \tag{24}$$

where λ is the half wavelength of the wrinkle.

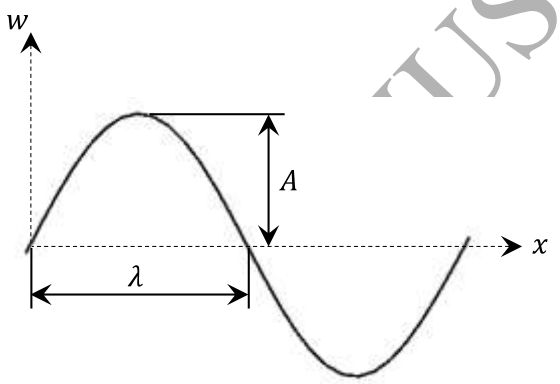

Fig. 18. Schematic of the half sine wave in the single wrinkle geometry.

Representing the wrinkle geometry by the sine function

$$w = A sin \frac{\pi x}{\lambda} \ , \tag{25}$$

and substituting Eq. (25) into Eq. (24), we obtain

$$l = \int_0^{\lambda} \sqrt{1 + \left(A \frac{\pi}{\lambda} cos \frac{\pi x}{\lambda}\right)^2}\, dx \ . \tag{26}$$

Taking the Taylor expansion of Eq. (26) and neglecting all terms above second order, l is approximately given by

$$l \approx \int_0^{\lambda} \left\{ 1 + \frac{1}{2} \left(A \frac{\pi}{\lambda} cos \frac{\pi x}{\lambda} \right)^2 \right\} dx \ , \tag{27}$$

where we have assumed the following condition:

$$A \frac{\pi}{\lambda} cos \frac{\pi \eta}{\lambda} \ll \ 1 \ . \tag{28}$$

Expanding Eq. (27), we obtain

$$A = \frac{2}{\pi} \sqrt{\lambda (l - \lambda)} \ . \tag{29}$$

Equation (29) represents the wrinkle amplitude as a function of the half-wavelength of the wrinkles and the length along the single wrinkle geometry. Here, the in-plane shrinkage strain in the wrinkled membrane is represented as a Green–Lagrange strain expression

$$\varepsilon_s = \frac{\lambda^2 - l^2}{2l^2} \ , \tag{30}$$

in which the length along the single wrinkle geometry is given by

$$l = \frac{\lambda}{\sqrt{2\varepsilon_s + 1}} \quad . \tag{31}$$

Substituting Eq. (31) into Eq. (29), we obtain

$$\frac{A}{\lambda} = \frac{2}{\pi} \sqrt{\frac{1}{\sqrt{2\varepsilon_s + 1}} - 1} \quad . \tag{32}$$

Equation (32) relates the in-plane shrinkage strain and the ratio of the wrinkle amplitude to the half-wavelength of the wrinkles.

Figures 19 and 20 compare the theoretical relation given by Eq. (32) with the relation observed in the experiment. The results in Fig. 19 were calculated from the in-plane shrinkage strain, the wrinkle amplitude and half-wavelength of wrinkles

measured along the central cross section. The wrinkle amplitude and the half-wavelength of wrinkles were calculated as follows. In Fig. 17, the intersections of the cross-sectional deformation shape of the membrane and $y = 0$ were calculated, and the half-wavelength of the single wrinkle was determined from the distance between two adjacent intersections. The wrinkle amplitude was calculated from the maximum or minimum value of the deformation shape in the single wrinkle. In Fig. 20, the results are plotted at different locations along the cross section of the membrane during all deformation steps. The points labeled "Edge" are located within 0.012 m of the real edge. In both figures, the actual relation plots below the theoretical relation. As the experimental wrinkle amplitude is likely to be below the actual amplitude due to the spatial resolution of the measured data (6 mm interval between the target points), the observed results are considered to be reasonable. Accordingly, the wrinkle strain is physically related to the ratio of the wrinkle amplitude to the half-wavelength of wrinkles, confirming that the actual formation mechanics of the wrinkles roughly obey inextensional theory.

The above discussion implies that even when the initial membrane surface is not uniformly flat, the in-plane shrinkage strain (wrinkle strain) defined by tension field theory physically agrees with the actual in-plane shrinkage of the wrinkled membrane. In addition, the wrinkle formation can be described by inextensional theory, and the wrinkle strain is physically related to the ratio of the wrinkle amplitude to the half-wavelength of the wrinkles.

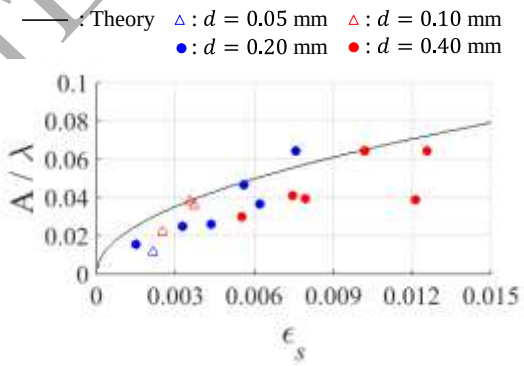

Fig. 19. Relation between the in-plane shrinkage strain and the ratio of the wrinkle amplitude to the half-wavelength of wrinkles. Black solid line and colored symbols denote the theoretical and experimental results, respectively.

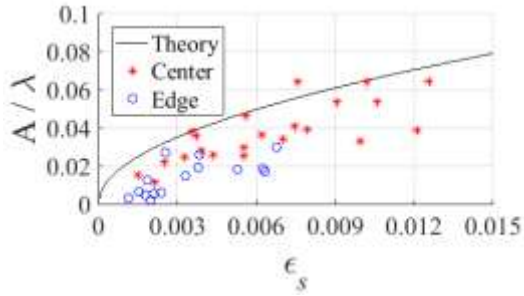

Fig. 20. Relation between the in-plane shrinkage strain and the ratio of the wrinkle amplitude to the half-wavelength of wrinkles at different cross sectional locations in the all steps. Black solid line denotes the theoretical result.

5. CONCLUSIONS

This study has clarified the physical correspondence relation of the membrane surface features and the wrinkle strain given by tension field theory through the comparison of the experimentally observed wrinkling phenomena quantitatively. The wrinkling phenomena on a rectangular membrane subjected to shear loading were analyzed experimentally by photogrammetry using the direct linear transformation method, and theoretically by a finite element analysis based on tension field theory. The major findings are summarized below.

1) In the wrinkling analysis based on tension field theory, the membrane surface features in the wrinkled region were located in the vicinity of the neutral surface bisecting the wrinkle geometry, even when the initial membrane surface is not uniformly flat. The difference, amounting to roughly 10% of the maximum wrinkle amplitude, is attributed to the experimental membrane being imperfectly fixed at the boundary.
2) The wrinkle strain, which releases the compressive stress in membranes in tension field theory, physically represents the in-plane shrinkage strain of the wrinkled membrane. This physical correspondence is confirmed regardless of the formation process of the wrinkles.
3) The formation mechanics of wrinkles roughly obey inextensional theory, and the wrinkle strain is physically related to the ratio of the wrinkle amplitude to the half-wavelength of the wrinkles.

ACKNOWLEDGEMENT

This work was partially supported by the Nohmura Foundation from Membrane Structure Technology. The experiment data used in this paper were provided by S. Kobayashi, former undergraduate student at the Tottori University. Author deeply appreciates their help.

REFERENCES

Abdel-Aziz, Y.I., 1971. Direct linear transformation from comparator coordinates into object space coordinates in close-range photogrammetry. Proc. the Symposium on Close-Range Photogrammetry, Am. Soc. Photogramm. 81, 103–107.

Akita, T., 2004. Research on wrinkling analysis of membrane structures using projection matrix (Ph.D dissertation). University of Tokyo, Japan. (in Japanese)

Akita, T., Nakashino, K., Natori, M.C., Park, K.C., 2007. A simple computer implementation of membrane wrinkle behavior via a projection technique. International J. Numerical Methods in Eng. 71, 1231–1259.

Akita, T., Natori, M.C., 2008. Sensitivity Analysis Method for Membrane Wrinkling Based on the Tension-Field Theory. AIAA J. 46, 1516–1527.

Fu, B., Sperber, E., Eke, F., 2016. Solar sail technology—A state of the art review. Prog. Aerosp. Sci.

Gardner, J.P., Mather, J.C., Clampin, M., Doyon, R., Greenhouse, M.A., Hammel, H.B., Hutchings, J.B., Jakobsen, P., Lilly, S.J., Long, K.S., Lunine, J.I., Mccaughrean, M.J., Mountain, M., Nella, J., Rieke, G.H., Rieke, M.J., Rix, H.-W., Smith, E.P., Sonneborn, G., Stiavelli, M., Stockman, H.S., Windhorst, R.A., Wright, G.S., 2006. The James Webb Space Telescope. Space Sci. Rev. 123, 485–606.

Iwasa, T., Natori, M.C., Higuchi, K., 2004. Evaluation of Tension Field Theory for Wrinkling Analysis With Respect to the Post-Buckling Study. J. Appl. Mech. 71, 532–540.

Lan, L., Wang, C.-G., Tan, H.-F., 2014. Experiment and evaluation of wrinkling strain in a corner tensioned square membrane. Acta Mechanica Sinica 30, 430-436.

Lecieux, Y., Bouzidi, R., 2010. Experimental analysis on membrane wrinkling under biaxial load – Comparison with bifurcation analysis. Int. J. Solids. Struct. 47, 2459–2475.

Lee, K., Lee, S.W., 2006. Analysis of Gossamer Structures Using Assumed-Strain Solid-Shell Finite Elements. J. Spacecr. Rockets 43, 1301-1307.

Lu, P., Hangai, Y., Kawaguchi, K.i., 1998. The Analysis of Wrinkling in Rectangular Tensioned Membrane Structures. Research Report on Membrane Structures, Membr.

Struct. Assoc. Jpn. 37–42.
Nayyar, V., Ravi-Chandar, K., Huang, R., 2014. Stretch-induced wrinkling of polyethylene thin sheets: Experiments and modeling. International Journal of Solids and Structures 51, 1847-1858.
Mansfield, E.H., 1970. Load Transfer Via a Wrinkled Membrane. Proceedings of the Royal Society of London. Series A, Math. Phys. Sci. 316, 269–289.
Mikulas, M.M., 1964. Behavior of a flat stretched membrane wrinkled by the rotation of an attached hub. National Aeronautics and Space Administration, Washington, D.C.
Miller, R.K., Hedgepeth, J.M., Weingarten, V.I., Das, P., Kahyai, S., 1985. Finite element analysis of partly wrinkled membranes. Comput. Struct. 20, 631–639.
Miyamura, T., 2000. Wrinkling on stretched circular membrane under in-plane torsion:: bifurcation analyses and experiments. Eng. Struct. 22, 1407–1425.
Nakashino, K., Natori, M.C., 2006. Three-Dimensional Analysis of Wrinkled Membranes Using Modification Scheme of Stress-Strain Tensor. AIAA J. 44, 1498–1504.
Roddeman, D.G., 1991. Finite-element analysis of wrinkling membranes. Commun. Appl. Numer. Methods 7, 299-307.
Santiago-Prowald, J., Baier, H., 2013. Advances in deployable structures and surfaces for large apertures in space. CEAS Space J. 5, 89–115.
Senda, K., Petrovic, M., Nakanishi, K., 2015. Localized Wrinkle Behavior near Fixed Boundaries in Flat and Cylindrical Membranes. J. Spacecr. Rockets 52, 1074-1090.
Steigmann, D.J., 1990. Tension-Field Theory. Proc. R. Soc. Lond. A. Math. Phys. Sci. 429, 141–173.
Stein, M., Hedgepeth, J.M., 1961. Analysis of Partly Wrinkled Membrane. National Aeronautics and Space Administration, Washington, D.C.
Wagner, H., 1931a. Flat sheet metal girders with very thin metal web. Part I : general theories and assumptions. NACA Tech. Memo. 604. 20, 200–207.
Wagner, H., 1931b. Flat sheet metal girders with very thin metal web. Part II : sheet metal girders with spars resistant to bending - oblique uprights - stiffness. NACA Tech. Mem. 605. 20.
Wagner, H., 1931c. Flat sheet metal girders with very thin metal web. Part III : sheet metal girders with spars resistant to bending - the stress in uprights - diagonal tension fields. NACA Tech. Memo. 606. 20, 281–284.
Wang, C., Du, X., Wan, Z., 2007. An Experimental Study on Wrinkling Behaviours and Characteristics of Gossamer Space Structures. Strain 43, 332–339.
Wong, Y., Pellegrino, S., 2006a. Wrinkled membranes-Part1: experiments. J Mech

Mater Struct 1, 3–25.
Wong, Y., Pellegrino, S., 2006b. Wrinkled membranes-Part3: Numerical Simulations. J Mech Mater Struct 1, 63–95.
Woo, K., Jenkins, C.H., 2013. Effect of Crease Orientation on Wrinkle–Crease Interaction for Thin Membranes. J. Spacecr. Rockets 50, 1024–1034.
Zienkiewicz, O.C., Taylor, R.L., Zhu, J.Z., 2005. 19 - Computer procedures for finite element analysis, The Finite Element Method Set (Sixth Edition). Butterworth-Heinemann, Oxford, pp. 664–667.

Biography of Author

Takashi IWASA was born in Shimane prefecture, Japan, in 1971. He received the B.E degree in structure engineering from Nagasaki University, Japan, in 1994, and M.E. degree in civil engineering from University of Tokyo, Japan, in 1996. Then, he gained employment with Penta–Ocean Construction Co., Ltd. In 2004, he received Doctor of Engineering in aeronautics and astronautics engineering from University of Tokyo, Japan.

In 2004, he joined the Institute of Space and Astronautical Science as a research collaborator. In 2005, he worked in Tokyo Institute of Technology as a Post–Doctoral Fellow, and became an invited scientist in Japan Aerospace and Exploration Agency in the same year. Since 2009, he has been working in Tottori University as an associate professor in the department of mechanical and aerospace engineering.

His current research interest includes gossamer space structure, precise–large space structure, structural mechanics, finite element analysis and photogrammetric measurement. Dr. Iwasa is a member of The Japan Society for Aeronautical and Space Sciences (JSASS), The Japan Society of Mechanical Engineering (JSME), The Japan Society for Experimental Mechanics (JSEM), The American Institute of Aeronautics and Astronautics (AIAA) and Membrane Structure Association of Japan. He was the recipient of the award for the research report on membrane structure in 2008.